Journal of Power Sources 240 (2013) 212–218

Contents lists available at SciVerse ScienceDirect

Journal of Power Sources

journal homepage: www.elsevier.com/locate/jpowsour

Short communication

Decoration of graphene with silicon nanoparticles by covalent immobilization for use as anodes in high stability lithium ion batteries

Guangyu Zhao [b], Li Zhang [b], Yufeng Meng [b], Naiqing Zhang [a,b], Kening Sun [a,b,*]

[a] State Key Laboratory of Urban Water Resource and Environment, Harbin Institute of Technology, Harbin, Heilongjiang 150090, PR China
[b] Academy of Fundamental and Interdisciplinary Sciences, Harbin Institute of Technology, Harbin, Heilongjiang 150080, PR China

HIGHLIGHTS

- Si nanoparticle–graphene hybrids were fabricated by covalent immobilization.
- High dispersion of Si nanoparticles and graphenes were obtained.
- The Si–graphenes exhibited good cycle stability for lithium ion battery anodes.

ARTICLE INFO

Article history:
Received 20 November 2012
Received in revised form
4 April 2013
Accepted 8 April 2013
Available online 18 April 2013

Keywords:
Lithium ion battery
Anode
Silicon nanoparticles
Graphene
Covalent immobilization

ABSTRACT

Si nanoparticle–graphene hybrids are fabricated by covalent immobilization and subsequent heating in a H_2 + Ar atmosphere. The absence of a graphite (002) peak in X-ray diffraction shows that the hybrid synthesized by this approach prevents graphene nanosheets re-agglomerating. Transmission electron microscopy shows a homogeneous distribution of Si nanoparticles on the graphene. Galvanostatic charge/discharge tests demonstrate that the Si nanoparticle–graphene hybrid has much better charge capacity retention than pristine Si nanoparticles and a Si nanoparticle/graphene mixture. The relationship of the capacity to the weight ratio of Si nanoparticles and graphene in the hybrid has been investigated. The results reveal that the hybrid of with a weight ratio 15:1 (Si:G) exhibits the most stable cycle performance, which retains 92.7% capacity of the 1st cycle after 50 charge/discharge cycles. The 1st Li^+ insertion capacity is 1297 mAh g^{-1}, and the 50th Li^+ insertion capacity is 1203 mAh g^{-1}.

1. Introduction

The possibility of applying rechargeable lithium ion batteries in mobile and stationary power storage has generated numerous studies to improve their energy density, power density and cycle life. One active research area is to replace graphite as the energy storage component in the anode with materials of higher storage capacity. Si has attracted much attention as anode material for its high theoretical capacity (4200 mAh g^{-1}). However, the poor cycle performances resulting from the low intrinsic electronic conductivity and the large volume change in Li^+ insertion/extraction process hampers its practical implementation [1]. Various forms of Si electrode materials have been explored to overcome these disadvantages [2–10], such as Si nanotubes [2–4] and nanowires [5,6] by chemical vapour deposition, Si nanofilms [10] by electrodeposition. According to these previous literatures, constructing sufficient inner-space for Si grains to accommodate the volume expansion during Li^+ insertion is a universal strategy. However, these studies are still not satisfactory, either because of high cost manufacturing, and/or low output for practical implementation. Therefore, there is a critical need to design a Si-based electrode with high Si grains' dispersion using a more accessible method.

Graphene having high conductivity, high mechanical strength, and super-high specific surface area [11–21], is a good candidate as fillers to construct inner-space for Si materials [22,23]. In addition, the low cost starting material and the readily scalable preparation process also bring graphenes a promising commercial prospect for their practical application. However, the homogeneous dispersion of Si grains and graphenes in the material is the prerequisite of generating sufficient inner-space. In this study, monolayer Si nanoparticles (SNs) were firmly anchored on graphene oxides (GOs) by covalent immobilization. Then, the as-synthesized Si–GO

* Corresponding author. State Key Laboratory of Urban Water Resource and Environment, Harbin Institute of Technology, Harbin, Heilongjiang 150090, PR China. Tel./fax: +86 451 86412153.
E-mail address: keningsun@yahoo.com.cn (K. Sun).

0378-7753/$ – see front matter © 2013 Elsevier B.V. All rights reserved.
http://dx.doi.org/10.1016/j.jpowsour.2013.04.025

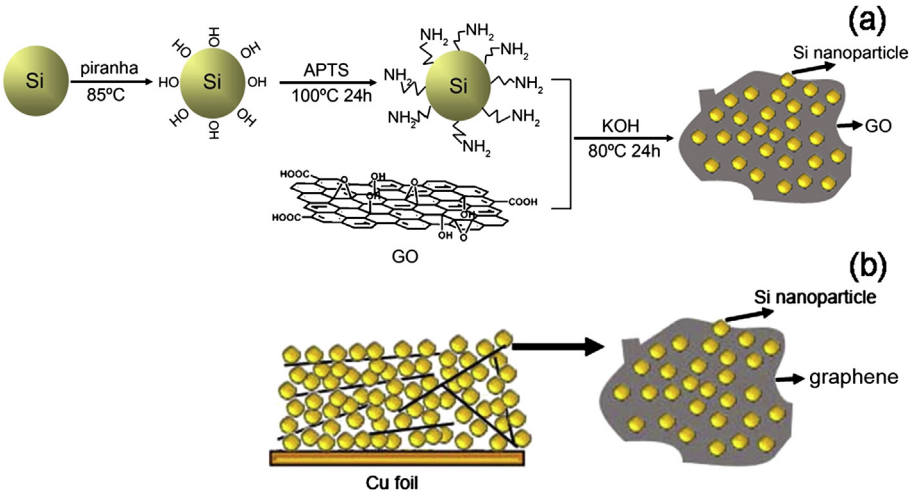

Fig. 1. (a) Scheme of fabricating Si–GO hybrid and (b) Si–graphene anode.

hybrid was reduced to Si–graphenes in H_2 5% + Ar 95% atmosphere. This process caused a uniform dispersion of SNs on graphene surface, prevented SNs aggregating and the irreversible agglomerates of the graphenes in the following battery assembling.

2. Experimental

2.1. Preparation of the Si–graphene hybrid

All the reagents in the experiments were analytical pure. GOs were prepared by oxidizing graphite using the improved Hummers method [24–28] (The details are shown in supplementary material). Si crystalline powder (Alfa Aesar, APS 0.05–0.1 μm) was first cleaned for 0.5 h in a piranha solution (2:1 in volume, H_2SO_4/H_2O_2) at 85 °C, followed by rinsing with copious amounts of deionized water and ethanol. Then, the Si powder was dried in an oven overnight. The pretreated Si (0.2 g) and 0.2 mL (3–aminopropyl)triethoxysilane (APTES) were dispersed in ethanol by ultrasonic 0.5 h. The mixture was stirred for 24 h at 100 °C. After cooling to room temperature, GOs and 0.05 g KOH were added into the flask. The mixture was treated in ultrasonic for 0.5 h and then stirred at 80 °C continuously for 24 h, filtered, and washed with deionized water and ethanol. The resulting Si–GO hybrid powder was dried in the oven at 50 °C overnight. The process of fabricating

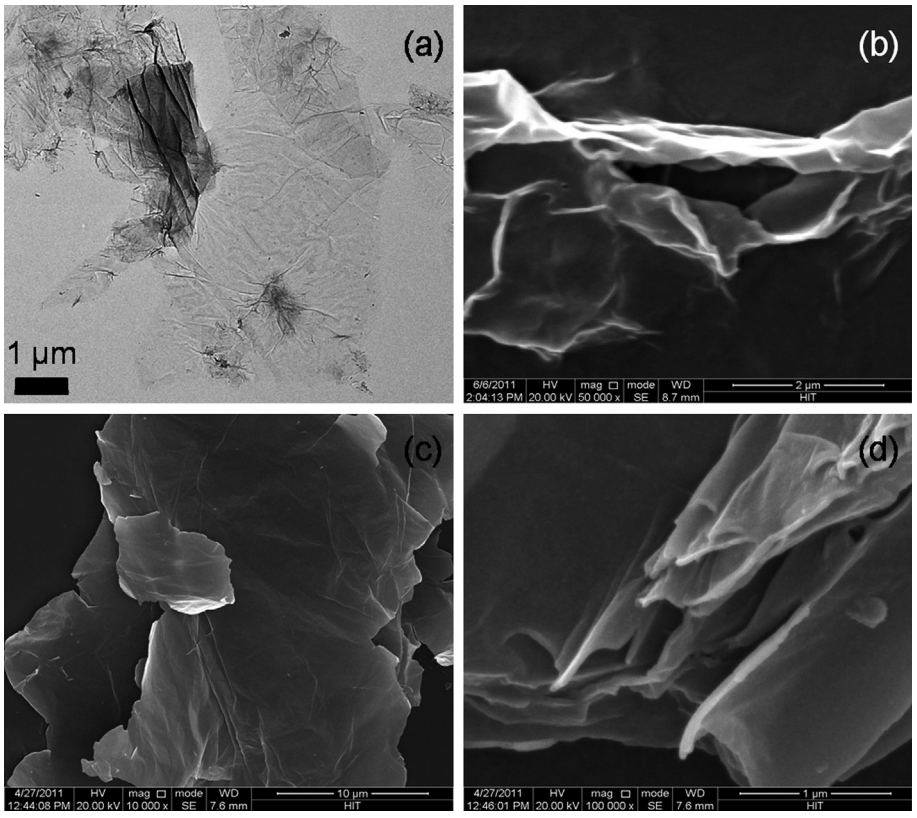

Fig. 2. (a) TEM and (b) SEM images of GOs, and (c, d) SEM of graphenes reduced from GOs directly in H_2 + Ar atmosphere.

Si–GO hybrid was shown in Fig. 1a. Si–graphene hybrid was obtained by treating Si–GO in H_2 5% + Ar 95% atmosphere at 700 °C for 3 h. The heat-treating temperature was decided according to the thermogravimetry (TG) curve in Fig. S1.

2.2. Structural and electrochemical characterization

A field-emission scanning electron microscope (FEI, Quanta 200f) was used to obtain scanning electron microscope (SEM) images of the materials. Transmission electron microscope (TEM) and energy dispersive spectrum (EDS) were obtained on a FEI Tecnai G^2. X-ray photoelectron spectroscopy (XPS) data were obtained with a K–Alpha electron spectrometer from Thermofish Scientific Company using AlK (1486.6 eV) radiation (The base pressure was about 1×10^{-8} mbar. The binding energies were referenced to the C1s line at 284.8 eV from adventitious carbon.). X–ray diffraction (XRD) patterns were obtained by Rigaku D/max-2000 X-ray diffractometer with Cu Kα radiation ($\lambda = 1.5418$ Å). TG of the precursor was performed with a thermal analysis instrument (Netzsch, STA449C) at a heating rate of 5 °C min^{-1} in H_2 5% + Ar 95% atmosphere.

Electrochemical measurements were carried out in the CR2025 button testing batteries using a two electrode electrochemical cell consisting of a Si-based electrode, two sheets of microporous membrane (Celgard 2400) and lithium foil as the counter electrode. Si-based electrode area of 154 mm^2 coated on Cu foils were used for electrochemical measurements (Si–graphene hybrid: PVDF: acetylene black = 6: 3: 1, weight ratio). The imaginable structure of Si–graphene anodes is showed in Fig. 1b. For comparison, pristine SNs and a Si/graphene mixture were also assembled in model batteries

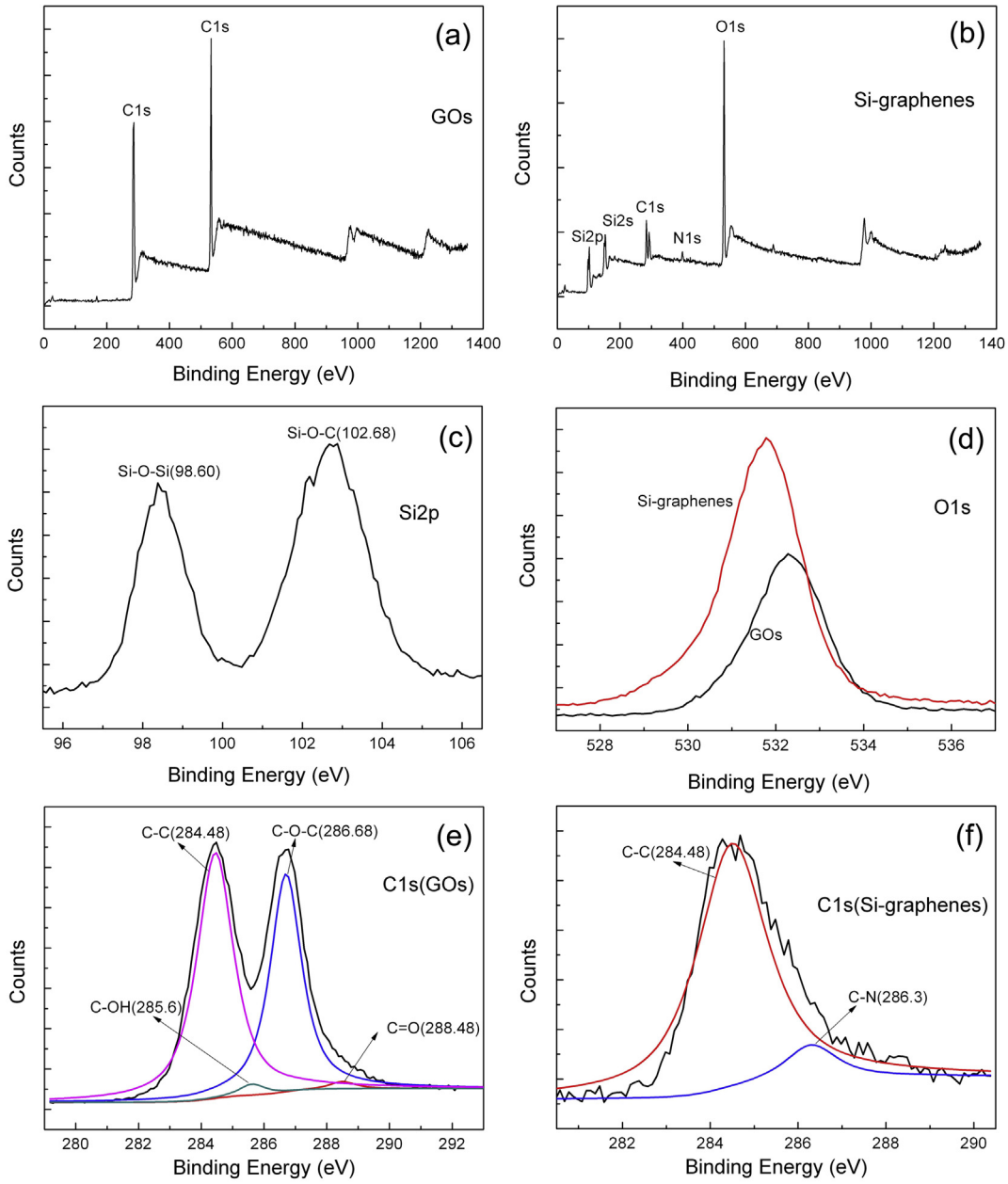

Fig. 3. XPS patterns of GOs and Si–graphene hybrid: survey curves of GOs (a) and Si–graphenes (b), high resolution curve of Si2p in Si–graphenes (c), high resolution curves of O1s in GOs and Si–graphenes (d), high resolution curves of C1s in GOs (e) and Si–graphenes (f).

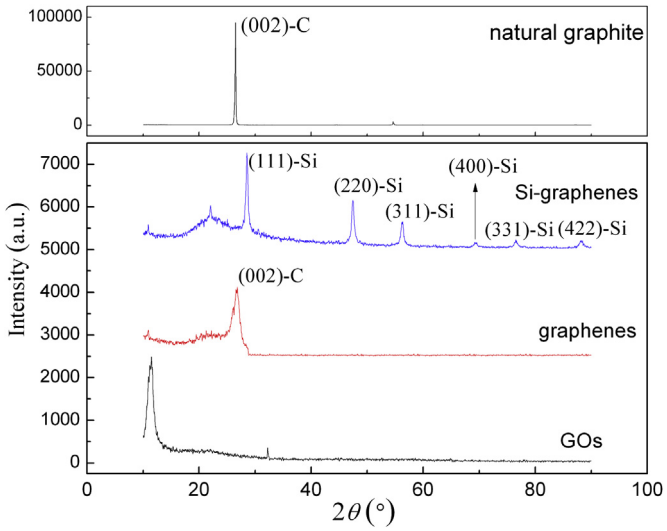

Fig. 4. XRD patterns of natural graphite, GOs, graphenes (reduced from GOs directly), and Si–graphene hybrid.

to measure the electrochemical characteristic. Si/graphene mixture was prepared by mixing SNs with GOs directly and subsequent filtering, drying, heating in H_2 + Ar atmosphere. The model battery electrolyte was $LiPF_6$ (1 M) in a 50: 50 (V/V) mixture of ethylene carbonate (EC) and dimethyl carbonate (DMC) provided by Tinci Company (Guangzhou China). A BTS-2000 Neware Battery Testing System was employed for galvanostatic charge/discharge tests. A PAR 2273 electrochemical workstation was used for the electrochemical impedance spectroscopy (EIS) measurements.

3. Results and discussion

TEM and SEM images in Fig. 2a, b and the pictures in Fig. S2 indicate the well dispersed GOs. The TEM image (Fig. 2a) reflects that the obtained GOs are in micrometer scale. There are plenty of folds on the GOs in the SEM image (Fig. 2b), which means the well dispersed GOs are monolayer or few layer nanosheets. The images in Fig. 2c and d are the graphenes reduced directly from GOs in H_2 + Ar atmosphere, in which the reduced GOs have fewer folds than GOs and stacked together to a multilayer stacking. The re-stacking of graphenes can be attributed to the disappearance of charge repulsion, when they are reduced from GOs. According to the above analysis, the graphenes will regress to the stack state after reduced in the mix atmosphere, if there is no intercalation substance in the graphene layers. Therefore, the Si–graphene hybrid was prepared in liquid phase after a strong ultrasonic dispersion. The covalent immobilization guarantees the SNs anchoring on the graphenes stably, which act as the intercalation substance in the subsequent heat treating reducting.

XPS results of GOs and Si–graphene hybrid in Fig. 3 reveal the successful decoration of SNs on GOs. The survey of GOs in Fig. 3a shows the absence of any detectable amounts Si and N1s. Compared with GOs, the survey of Si–graphenes in Fig. 3b shows the presence of Si2p and N1s originating from SNs and APTES. As shown in Fig. 3c, a strong band of Si2p appears 102.68 and 98.60 eV, assigning to Si–O–C and Si–O–Si, respectively. Fig. 3d shows O1s XPS spectrum evolution of GOs to Si–graphenes, which demonstrate the chemical bond transformation of O element. The O1s in GOs appeared at 532.28 eV, assigning to O in C–O–C and C=O. Then in the Si–graphenes, the O1s appeared at 531.78 eV, assigning to O in C–O–Si/Si–O–Si, and C=O [29]. The high resolution data of C1s area of the GOs and Si–graphenes are shown in Fig. 3e and f.

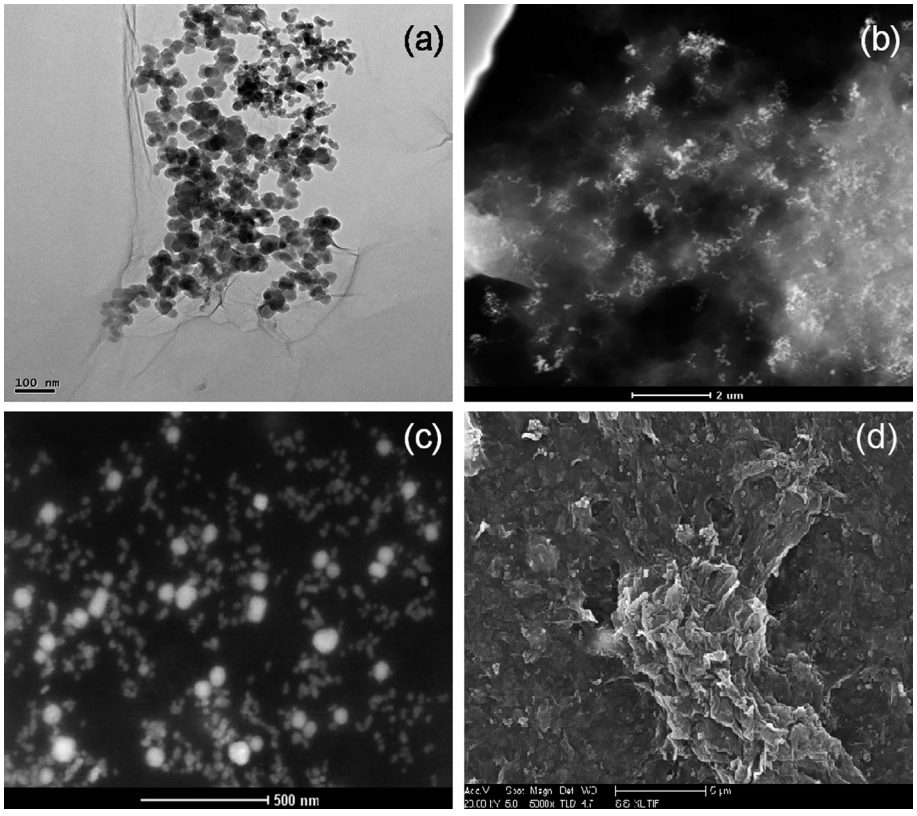

Fig. 5. (a) TEM images and (b, c) dark field images of Si–graphenes, (d) SEM image of Si–graphenes in the anodes.

Fig. 3e clearly indicates a considerable degree of oxidation with four components corresponding to carbon atoms in different functional groups: the C–C in graphene layer (284.48 eV), the C in C–OH (285.6 eV), the C in C–O–C (286.68 eV) and the C in C=O (288.48 eV). However, in the C1s of Si–graphenes (Fig. 3f), there is an additional component at 286.3 eV assigning to C bound with nitrogen [25,30], strongly indicating that the amino moieties reaction with the epoxy groups on GOs.

The dispersion of graphenes in the as-prepared Si–graphene hybrid can be investigated by the XRD patterns of natural graphite, GOs, graphenes and Si–graphene hybrid in Fig. 4. The peak at 27° in the pattern of natural graphite can be assigned to the planes of (002). The (002) peak disappears in the pattern of GOs, and the characteristic peak at 10–12° can be assigned to the widening interlayer spacing by functional groups. The stacking of multilayer graphenes, that reduced directly from GOs in H_2 + Ar atmosphere, make the characteristic peak at 10–12° to be weak because of the narrowed down interlayer spacing. Meanwhile, the (002) peak increases visibly, but its intensity is much lower than natural graphite. The XRD pattern of the graphenes also shows a broad peak at 20–25° indicating the disordered agglomerating of graphene nanosheets. This means that the graphenes are the mixture of crystalline and disordered graphite, which is consistent with the SEM results in Fig. 2d. In the pattern of the Si–graphene hybrid, there is no (002) peak but the broad peak at 20–25°, showing no graphene sheet stacking in Si–graphene hybrid powder. Based on the above analysis, the method in this study to fabricate Si–graphene hybrid allows for a good dispersion of graphenes. Except the broad peak, all the diffraction peaks in the XRD pattern of the Si–graphene can be indexed as a pure diamond cubic crystal structure of Si with cell constant 5.43 Å (JCPDS card No. 27-1402).

The TEM image in Fig. 5a shows a monolayer SNs spreading on the graphene layer. It is hard to make a distinction between the graphenes and the carbon-supported film on the copper grid as the extremely thin graphenes. In the dark field images of Si–graphene hybrid (Fig. 5b, c), the white particles are SNs, and the white "fog" is graphenes. Obviously, all the SNs are decorated on the graphenes that, no white particle is in the black area of Fig. 5b. Moreover, as shown in the high-magnification image of Fig. 5c, the dispersion of the SNs on graphenes are so homogeneous that no aggregated detected. SEM image of Si–graphenes on the current collector (Fig. 5d) shows an obvious improvement of SNs' dispersion compared with the SN anode in Fig. S3. The good dispersion of SNs on Si–graphenes let more inner space to distribute in the anodes, as seen in Fig. 1b, which is the reason of the following better cycle performances.

The cycle performances of the pristine SNs and Si/graphene mixture are supplied in Fig. 6. Obviously, the Si/graphene mixture has better stability than the pristine SNs, which have an obvious agglomeration in the anodes (Fig. S3). The better stability of Si/graphene mixture than SNs illustrates the graphenes work indeed for improving the performances of SNs. Nevertheless, the capacity of the mixture decreases continuously, because the uniform dispersion cannot be achieved in Si/graphene mixture, the volume change cannot be accommodated effectively and the conductive network cannot disperse well in anodes.

The cycle performances of Si–graphene hybrids in different SN, graphene ratios are displayed in Fig. 7. Visibly, all hybrids have better capacity retention than the Si/graphene (Fig. 6) mixture, because of better dispersion of SNs in the hybrids. The synthesis process of the hybrids with a covalent immobilization assistant approach leads the SNs dispersing well on the graphenes, which guarantees there is abundant interspace between the SNs. The abundant interspace can accommodate the volume swing of SNs in the charge/discharge processes effectively, which let the Si-based

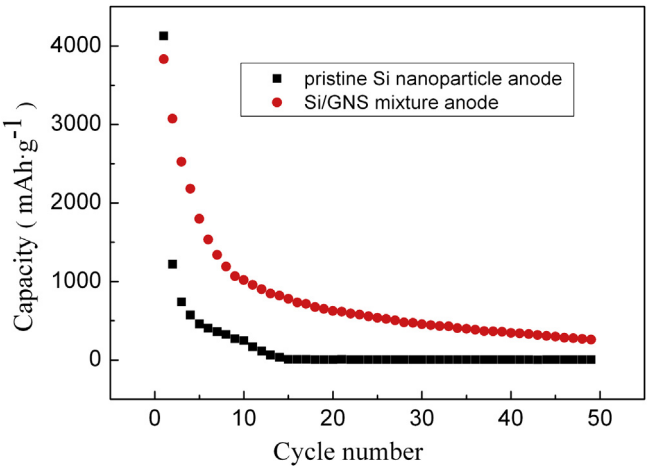

Fig. 6. Cycling performances (Li^+ insertion capacities) of the pristine SN anode and Si/graphene mixture anode.

anodes to maintain stable in cycling. The initial Li^+ insertion capacities of the Si–graphene hybrid are 1234, 1260, 1297, 1353, 1403 mAh g^{-1} for Si:GNS = 5:1, 10:1, 15:1, 20:1, 25:1 in weight ratio, respectively. The Li^+ extraction capacities are 765, 770, 973, 908, 618 mAh g^{-1} for different ratios, as seen from the discharge–charge curves of initial 10 cycles in Fig. S4. The first cycle irreversible capacity loss mainly originated from the reduction of the electrolyte, resulting in the formation of the solid electrolyte interphase (SEI) film on the surface of the SNs and the graphenes or from irreversible Li^+ insertion into the hybrid.

The Li^+ insertion capacities of the Si–graphene hybrid anodes are 737, 882, 1203, 860, 258 mAh g^{-1} after 50 cycles for different ratios. The material of 15:1 exhibits the highest capacity after 50 cycles. The initial capacity of the sample 15:1 is 1297 mAh g^{-1}, and this value falls to 1110 mAh g^{-1} at second cycle (Fig. 8). Then, it gradually increases to 1203 mAh g^{-1} at the 50th cycle. The high reserve rate of sample 15:1 after 50 cycles (92.7% of the 1st cycle) is a significant improved property compared with those Si and graphene hybrid materials obtained by others [31–36]. The possible reasons for the capacity decreasing at first and then increasing are given below. Some SNs were sandwiched by two graphene layers to form a graphene–Si–graphene stacking, resulting in the electrolyte could not infiltrate into the "sandwiches". With the interspace largened by the volume expanded SNs in the Li^+ insertion, the

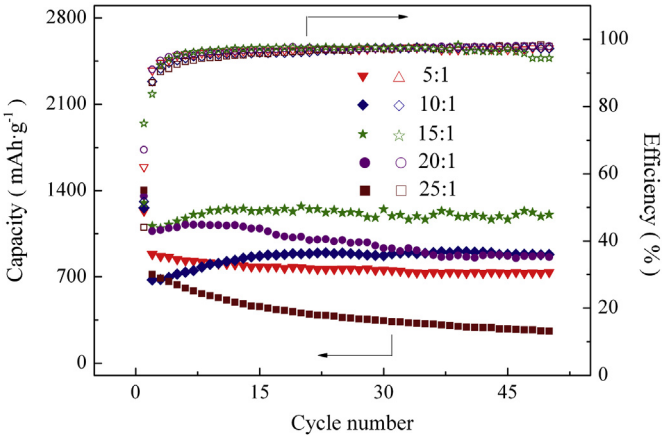

Fig. 7. Cycle performances (Li^+ insertion capacities) and the coulombic efficiencies of the Si–graphene hybrid in different weight ratios. The charge/discharge conditions are 1.5–0.02 V, 150 mA g^{-1} (Corresponding to 0.2 C).

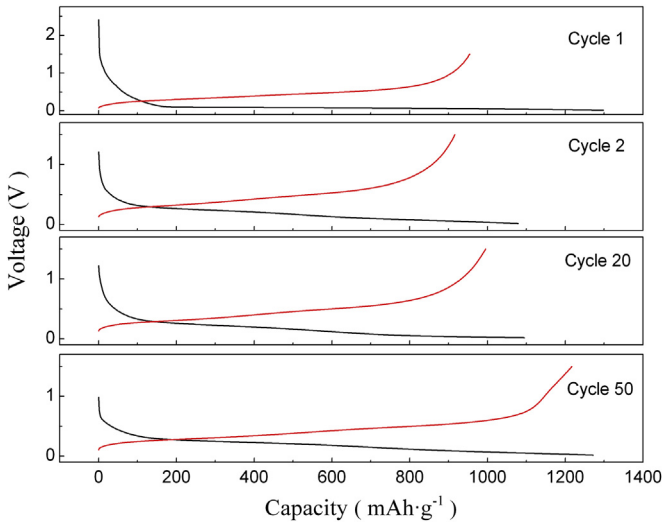

Fig. 8. Charge/discharge curves of the Si–graphene hybrid (15:1) anodes at the 1st, 2nd, 20th, and 50th cycles.

electrolyte infiltrated into the "sandwiches". Thus, after several cycles, capacity reached a stable state when the materials steady. The course of capacity increasing for the sample of 15:1 also can be verified by the EIS results, in which the high frequency semicircles related to the properties of electrochemical reaction resistant keeps decreasing after the 1st cycle, as seen in Fig. S5.

Nevertheless, only the hybrid with ratios of 10:1, 15:1, and 20:1 have the course of capacity decreasing at first and then increasing. There is not the course for the hybrid of 5:1 and 25:1, as seen in Fig. S4. This means that the cycle performances of the Si–graphene hybrid are visibly influenced by the concentration of the graphenes in the hybrid, which affects the SN dispersion severely. The materials exhibit a low capacity when there are more graphenes due to the lower content of SNs. On the contrary, the materials have a larger initial capacity. But the capacity decreases gradually like the pristine SNs, because there are not enough graphenes to construct the frame work, which resulting in the SNs aggregating. Thus, the material of 25:1 has the largest initial capacity, but the worst cycle performances in all the ratios.

The C-rate performances of the samples in 15:1 have been measured, and shown in Fig. 9. The batteries behave a reversible

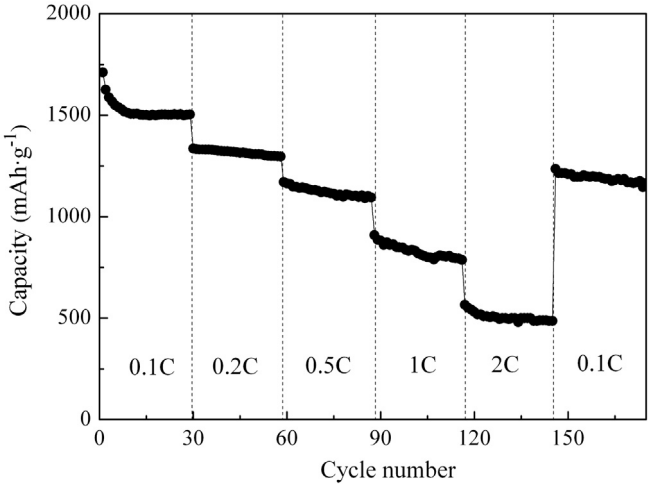

Fig. 9. C-rate performances of Si–graphene hybrid (15:1).

capacity of 800 and 500 mAh g^{-1}, when the current density increases to 1 C and 2 C, respectively. Furthermore, the capacity still maintains more than 1200 mAh g^{-1}, when the current density returns to 0.1 C after cycling at the high current densities.

4. Conclusion

Si–graphene hybrid, that exhibited a homogeneous distribution of SNs on the graphene nanosheets, was synthesized by covalent immobilization and subsequent heating in H_2 + Ar atmosphere. The homogeneous distribution of Si nanoparticles and the super high surface area of graphenes supplied the hybrid enough internal space to accommodate the volume expansion in the Li^+ insertion. Otherwise, the high mechanical strength and conductivity of graphenes led the hybrid a good structural stability and electronic conductivity. All these resulted in a high stable cycle performance when the hybrid was as anode material for lithium ion batteries. The capacity of the Si–graphene hybrid anode at the 50th cycle still retained 1203 mAh g^{-1}, which was 92.7% of the 1st cycle.

Graphenes have many advantages in mechanics and electronics. Furthermore, they can be made from a low cost starting material and the preparation process is also cheap and readily scalable. Therefore, graphenes are attractive filler for the materials in energy storage, optoelectronics, and catalysis, etc. The approach of connecting–OH on the materials and the oxygen functional groups on GOs by chemical reaction can be applied to the other materials decorated on graphenes. The graphenes can be dispersed well in this chemical reaction method. This method may be a new avenue for the preparation of the graphenes functionalized with various nanoparticles and creates a new class of graphene–based hybrid with unique properties for potential applications.

Acknowledgements

This work was supported by the National Science Foundation of China (NSFC) (NO. 20903031), the China Postdoctoral Science Foundation, and the Development Program for Outstanding Young Teachers and the Fundamental Research Funds for the central University (NO. HIT. NSRIF. 2010 056), and the Open Project of State Key Laboratory of Urban Water Resource and Environment, Harbin Institute of Technology (Grant no. QA201026).

Appendix A. Supplementary data

Supplementary data related to this article can be found at http://dx.doi.org/10.1016/j.jpowsour.2013.04.025.

References

[1] U. Kasavajjula, C. Wang, A.J. Appleby, J. Power Sources 163 (2007) 1003–1039.
[2] T. Song, J. Xia, J.-H. Lee, D.H. Lee, M.-S. Kwon, J.-M. Choi, J. Wu, S.K. Doo, H. Chang, W. Il Park, D.S. Zang, H. Kim, Y. Huang, K.-C. Hwang, J.A. Rogers, U. Paik, Nano Lett. 10 (2010) 1710–1716.
[3] W. Wang, P.N. Kumta, Acs Nano 4 (2010) 2233–2241.
[4] M.-H. Park, M.G. Kim, J. Joo, K. Kim, J. Kim, S. Ahn, Y. Cui, J. Cho, Nano Lett. 9 (2009) 3844–3847.
[5] L.-F. Cui, Y. Yang, C.-M. Hsu, Y. Cui, Nano Lett. 9 (2009) 3370–3374.
[6] V.A. Krivchenko, D.M. Itkis, S.A. Evlashin, D.A. Semenenko, E.A. Goodilin, A.T. Rakhimov, A.S. Stepanova, N.V. Suetina, A.A. Pilevskya, P.V. Voronina, Carbon 50 (2012) 1422–1444.
[7] J. Saint, M. Morcrette, D. Larcher, L. Laffont, S. Beattie, J.-P. Peres, D. Talaga, M. Couzi, J.-M. Tarascon, Adv. Funct. Mater. 17 (2007) 1765–1774.
[8] C. Martin, M. Alias, F. Christien, O. Crosnier, D. Belanger, T. Brousse, Adv. Mater. 21 (2009) 4735–4742.
[9] J.S. Bridel, T. Azais, M. Morcrette, J.M. Tarascon, D. Larcher, Chem. Mater. 22 (2010) 1229–1241.
[10] H. Ma, F. Cheng, J. Chen, J. Zhao, C. Li, Z. Tao, J. Liang, Adv. Mater. 19 (2007) 4067–4070.
[11] M.J. Allen, V.C. Tung, R.B. Kaner, Chem. Rev. 110 (2010) 132–145.

[12] A.V. Murugan, T. Muraliganth, A. Manthiram, Chem. Mater. 21 (2009) 5004–5006.
[13] S. Park, K.-S. Lee, G. Bozoklu, W. Cai, S.T. Nguyen, R.S. Ruoff, Acs Nano 2 (2008) 572–578.
[14] M. Liang, L. Zhi, J. Mater. Chem. 19 (2009) 5871–5878.
[15] D.-W. Wang, F. Li, J. Zhao, W. Ren, Z.-G. Chen, J. Tan, Z.-S. Wu, I. Gentle, G.Q. Lu, H.-M. Cheng, Acs Nano 3 (2009) 1745–1752.
[16] H. Wang, H.S. Casalongue, Y. Liang, H. Dai, J. Am. Chem. Soc. 132 (2010) 7472–7477.
[17] E. Yoo, T. Okata, T. Akita, M. Kohyama, J. Nakamura, I. Honma, Nano Lett. 9 (2009) 2255–2259.
[18] G.M. Scheuermann, L. Rumi, P. Steurer, W. Bannwarth, R. Muelhaupt, J. Am. Chem. Soc. 131 (2009) 8262–8270.
[19] H.-P. Cong, J.-J. He, Y. Lu, S.-H. Yu, Small 6 (2010) 169–173.
[20] X. Huang, Z. Yin, S. Wu, X. Qi, Q. He, Q. Zhang, Q. Yan, F. Boey, H. Zhang, Small 7 (2011) 1876–1902.
[21] S. Yang, X. Feng, L. Zhi, Q. Cao, J. Maier, K. Muellen, Adv. Mater. 22 (2010) 838–842.
[22] J.K. Lee, K.B. Smith, C.M. Hayner, H.H. Kung, Chem. Commun. 46 (2010) 2025–2027.
[23] S. Yang, X. Feng, S. Ivanovici, K. Muellen, Angew. Chem. Int. Ed. 49 (2010) 8408–8411.
[24] W. Hummer, R. Offeman, J. Am. Chem. Soc. 80 (1958) 1339.
[25] S. Stankovich, D.A. Dikin, R.D. Piner, K.A. Kohlhaas, A. Kleinhammes, Y. Jia, Y. Wu, S.T. Nguyenb, R.S. Ruoff, Carbon 45 (2007) 1558–1565.
[26] Y. Zhu, S. Murali, W. Cai, X. Li, J.W. Suk, J.R. Potts, R.S. Ruoff, Adv. Mater. 22 (2010) 3906–3924.
[27] S. Stankovich, R.D. Piner, S.T. Nguyen, R.S. Ruoff, Carbon 44 (2006) 3342–3347.
[28] D.R. Dreyer, S. Park, C.W. Bielawski, R.S. Ruoff, Chem. Soc. Rev. 39 (2010) 228–240.
[29] H. Yang, F. Li, C. Shan, D. Han, Q. Zhang, L. Niu, A. Ivaska, J. Mater. Chem. 19 (2009) 4632–4638.
[30] R.J. Waltman, J. Pacansky, C.W. Bates, Chem. Mater. 5 (1993) 1799–1804.
[31] X. Zhou, Y.-X. Yin, L.-J. Wan, Y.-G. Guo, Adv. Energy Mater. 2 (2012) 1086–1090.
[32] S. Yang, G. Li, Q. Zhu, Q. Pan, J. Mater. Chem. 22 (2012) 3420–3425.
[33] X. Zhou, Y.-X. Yin, L.-J. Wan, Y.-G. Guo, Chem. Commun. 48 (2012) 2198–2200.
[34] J. Luo, X. Zhao, J. Wu, H.D. Jang, H.H. Kung, J. Huang, J. Phys. Chem. Lett. 3 (2012) 1824–1829.
[35] X. Xin, X. Zhou, F. Wang, X. Yao, X. Xu, Y. Zhu, Z. Liu, J. Mater. Chem. 22 (2012) 7724–7730.
[36] H.-C. Tao, L.-Z. Fan, Y. Mei, X. Qu, Electrochem. Commun. 13 (2011) 1332–1335.